INTERNATIONAL JOURNAL FOR NUMERICAL METHODS IN FLUIDS
Int. J. Numer. Meth. Fluids 2007; **53**:23–55
Published online 19 June 2006 in Wiley InterScience (www.interscience.wiley.com). DOI: 10.1002/fld.1242

An eigenvector-based linear reconstruction scheme for the shallow-water equations on two-dimensional unstructured meshes

Sandra Soares Frazão[1,*,†] and Vincent Guinot[2,‡]

[1]*Fonds National de la Recherche Scientifique and Université catholique de Louvain, Place du Levant, 1, B-1348 Louvain-la-Neuve, Belgium*
[2]*Hydrosciences Montpellier, UMR 5569 (CNRS, IRD, UM1, UM2), Université Montpellier 2, Maison des Sciences de l'Eau – MSE, 34095 Montpellier Cedex 5, France*

SUMMARY

This paper presents a new approach to MUSCL reconstruction for solving the shallow-water equations on two-dimensional unstructured meshes. The approach takes advantage of the particular structure of the shallow-water equations. Indeed, their hyperbolic nature allows the flow variables to be expressed as a linear combination of the eigenvectors of the system. The particularity of the shallow-water equations is that the coefficients of this combination only depend upon the water depth. Reconstructing only the water depth with second-order accuracy and using only a first-order reconstruction for the flow velocity proves to be as accurate as the classical MUSCL approach. The method also appears to be more robust in cases with very strong depth gradients such as the propagation of a wave on a dry bed. Since only one reconstruction is needed (against three reconstructions in the MUSCL approach) the EVR method is shown to be 1.4–5 times as fast as the classical MUSCL scheme, depending on the computational application. Copyright © 2006 John Wiley & Sons, Ltd.

Received 26 August 2005; Revised 8 March 2006; Accepted 19 March 2006

KEY WORDS: hyperbolic conservation laws; shallow-water equations; Godunov-type schemes; MUSCL scheme; higher-order reconstruction; unstructured grids

*Correspondence to: Sandra Soares Frazão, Fonds National de la Recherche Scientifique and Université catholique de Louvain, Place du Levant, 1, B-1348 Louvain-la-Neuve, Belgium.
†E-mail: soares@gce.ucl.ac.be
‡E-mail: guinot@msem.univ-montp2.fr

Contract/grant sponsor: Fonds National de la Recherche Scientifique (FNRS); contract/grant number: 2004/V 6/5/009-M 14/9/5-CS-20372 (Bourse de séjour scientifique)

1. INTRODUCTION

1.1. Motivation of the approach

The shallow-water equations describing the movement of water under the assumption of a hydrostatic pressure distribution form a system of hyperbolic equations. When solving those equations numerically in the context of fast transient flows, the numerical scheme is required to be shock capturing to be able to represent discontinuities arising from fast changing flow conditions. Godunov-type schemes, consisting of a finite-volume discretization of the equations written in integral form (both in space and time), are among the most widely used schemes. In the original Godunov method [1], the continuous system is discretized using piecewise constant data over each computational cell, and the numerical mass and momentum fluxes are computed at each time step across the interfaces between the cells.

A wide range of Godunov-type schemes have been developed for producing accurate numerical solutions of hyperbolic systems of partial differential equations in one dimension of space (see e.g. References [2–5] for a presentation of some classical methods). The most widely used approach is the MUSCL scheme (also called the variable extrapolation method by some authors [4]), introduced by Van Leer [2, 6] for constructing higher-order methods. It relies on the idea of modifying the piecewise constant data in the first-order Godunov method [1] into piecewise linear functions, where the values at the cell interfaces are thus extrapolated values [4]. The extension of second-order accurate schemes to two dimensions involves the construction of an appropriate linear representation of the solution within a computational cell, with a subsequent limiting in order to avoid spurious oscillations in the solution due to the presence of local extrema issued from the reconstruction process. Some existing techniques for reconstructing and limiting the local solution gradients are summarized in Reference [7], where a framework is presented for the construction of multidimensional slope limiting operators for two-dimensional MUSCL-type finite volume schemes on triangular grids. Note that adaptive limiters have been proposed to improve the accuracy of the method [8].

In the original approach [2, 6] and in classical applications of the MUSCL approach to non-linear systems of conservation laws such as the shallow-water equations, the linear reconstruction process is applied independently to each variable of the system. This involves a high computational cost to obtain second-order spatial accuracy: for the 2D shallow-water equations, the reconstruction process must be carried out three times at each time step. Moreover, common methods to achieve second-order accuracy in time such as the predictor–corrector sequence of Reference [9] require the characterization and solution of two Riemann problems at each computational time step.

The method proposed in the present paper is called the Eigenvector-based Reconstruction (EVR) hereafter. It makes use of the eigenstructure of the shallow-water equations to restrict the number of operations needed to achieve second-order accuracy. It is inspired by the generalized Riemann problem (GRP) approach of Ben-Artzi and Falcovitz [10] and Colella and Woodward's definition of the Riemann problem in the Eulerian PPM approach [3]. In the GRP approach, second-order accuracy in time is achieved by computing an averaged numerical flux over the time step, instead of using a predictor–corrector sequence. However, in these previous methods no use is made of the eigenstructure of the equations to simplify the computational procedure. The EVR approach as such was originally used in one-dimensional form for the simulation of two-phase flow in pipes [11, 12]. The present paper details its application to the solution of the two-dimensional shallow-

DOI: 10.1002/fld

water equations in the framework of the MUSCL reconstruction. Note however that the approach is not specific to the MUSCL reconstruction method and has been shown to be applicable to other reconstruction techniques (see e.g. References [11–13]). The advantages of the proposed approach over more classical higher-order reconstruction approaches when applied to the shallow-water equations are that: (i) reconstructing only the water depth is shown to yield numerical solutions, the quality of which is not significantly different from that of the classical MUSCL scheme, (ii) through an appropriate integration in time of the numerical flux over the time step [10, 14], second-order accuracy in time is achieved in a less expensive way than the classical predictor–corrector MUSCL approach, thus leading to a significantly faster method, and (iii) the independent reconstruction of the flow variables carried out in the classical MUSCL approach appears to yield spurious oscillations and stability problems near wetting or drying fronts, which is not the case for the EVR method (see Appendix A for an analysis of the problem).

The performance of the EVR method is assessed through comparison with the first-order Godunov scheme and with the MUSCL approach on two test cases. The first one consists of a circular dam-break problem on a flat bottom, with different ratios between the initial depths inside and outside the reservoir, respectively. The second test is a dam-break flow in a channel with a 90° bend, for which experimental data is available.

The present paper is organized as follows. The governing equations are recalled in Section 1. Section 2 gives the principles of the reconstruction of variables over unstructured grids and presents the classical MUSCL approach. Section 3 is devoted to the EVR reconstruction. Section 4 presents applications and compares the performances of the different approaches and Section 5 provides concluding remarks.

1.2. Governing equations

Godunov-type schemes aim to solve hyperbolic systems of conservation laws, such as the shallow-water equations stating mass and momentum conservation of a volume of water, that is systems of partial differential equations (PDEs) that can be written in the following vector form:

$$\frac{\partial \mathbf{U}}{\partial t} + \frac{\partial \mathbf{F}}{\partial x} + \frac{\partial \mathbf{G}}{\partial y} = \mathbf{S} \tag{1}$$

where $\mathbf{U}$ is the conserved variable, $\mathbf{F}$ and $\mathbf{G}$ are the fluxes in the x and y directions, respectively, and $\mathbf{S}$ represents the source terms. In the case of the shallow-water equations, those vectors read

$$\mathbf{U} = \begin{pmatrix} h \\ q_x \\ q_y \end{pmatrix}, \quad \mathbf{F} = \begin{pmatrix} q_x \\ q_x^2/h + gh^2/2 \\ q_x q_y / h \end{pmatrix}$$
$$nonumber$$
$$\mathbf{G} = \begin{pmatrix} q_y \\ q_x q_y / h \\ q_x^2/h + gh^2/2 \end{pmatrix}, \quad \mathbf{S} = \begin{pmatrix} 0 \\ (S_{0x} - S_{f,x})gh \\ (S_{0y} - S_{f,y})gh \end{pmatrix} \tag{2}$$

DOI: 10.1002/fld

where g is the gravitational acceleration, h is the water depth, q_x and q_y are the unit discharges in the x and y directions, respectively, $S_{0,x} = -\partial z_b/\partial x$ and $S_{0,y} = -\partial z_b/\partial y$ are the source terms related to the variation of the bed elevation z_b in the x and y directions, respectively, and $S_{f,x}$ and $S_{f,y}$ are the friction source terms in the x and y directions, respectively. The friction terms are classically computed using Manning's formula

$$S_{f,x} = \frac{n_{\mathrm{M}}^2 (u_x^2 + u_y^2)^{1/2} u_x}{h^{4/3}}$$
$$S_{f,y} = \frac{n_{\mathrm{M}}^2 (u_x^2 + u_y^2)^{1/2} u_y}{h^{4/3}} \tag{3}$$

where n_{M} is Manning's number, $u_x = q_x/h$ and $u_y = q_y/h$ are the x and y velocity, respectively. System (1) can be rewritten in non-conservation form as

$$\frac{\partial \mathbf{U}}{\partial t} + \mathbf{A}_x \frac{\partial \mathbf{U}}{\partial x} + \mathbf{A}_y \frac{\partial \mathbf{U}}{\partial y} = \mathbf{S} \tag{4}$$

with $\mathbf{A}_x$ and $\mathbf{A}_y$ being the Jacobian matrices of $\mathbf{F}$ and $\mathbf{G}$ with respect to $\mathbf{U}$

$$\mathbf{A}_x = \begin{bmatrix} 0 & 1 & 0 \\ c^2 - u_x^2 & 2u_x & 0 \\ -u_x u_y & u_y & u_x \end{bmatrix}, \quad \mathbf{A}_y = \begin{bmatrix} 0 & 1 & 0 \\ -u_x u_y & u_y & u_x \\ c^2 - u_y^2 & 0 & 2u_y \end{bmatrix} \tag{5}$$

and where $c = (gh)^{1/2}$ is the wave celerity. The system is hyperbolic because $\mathbf{A}_x$ and $\mathbf{A}_y$ have three distinct, real eigenvalues each. Such eigenvalues express the wave propagation speeds in the direction of concern. The eigenvalues in the x direction are:

$$\lambda^{(1)} = u_x - c$$
$$\lambda^{(2)} = u_x \tag{6}$$
$$\lambda^{(3)} = u_x + c$$

1.3. The six steps of Godunov-type schemes

Godunov-type schemes comprise the six following steps:

(1) Space is discretized into computational cells (Figure 1), also called volumes, over which the average value of the solution $\mathbf{U}$ is to be computed at each time step. The average value of $\mathbf{U}$ over the cell i at the time level n is denoted by $\mathbf{U}_i^n$.
(2) $\mathbf{U}$ is reconstructed in space over the computational cells. The reconstructed profile over the cell i at the time level n is denoted by $\widetilde{\mathbf{U}}_i^n(x, y)$. This function is determined from the average value $\mathbf{U}_i^n$ in the current cell and the averages $\mathbf{U}_j^n$ in the neighbouring cells. The way to obtain $\widetilde{\mathbf{U}}_i^n(x, y)$ will be detailed in Section 3.

DOI: 10.1002/fld

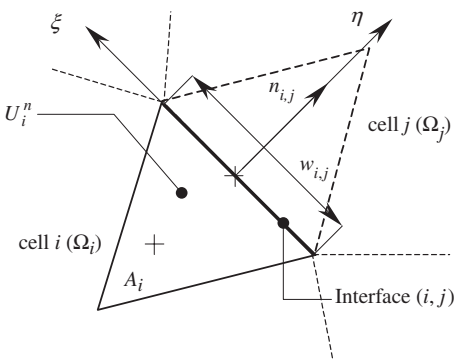

Figure 1. Definition sketch of the geometry and variables.

(3) At the interfaces between the computational cells, the discontinuities generated by the reconstructed profiles form GRPs. These GRPs are converted into equivalent Riemann problems (ERPs) in the direction normal to the interfaces.
(4) Solving the ERP at each interface provides the value of **U** (and therefore **F** and **G**) at the interfaces between the cells. The ERPs can be solved using standard, one-dimensional Riemann solvers.
(5) The solution is advanced in time using the balance equation

$$\mathbf{U}_i^{n+1} = \mathbf{U}_i^n - \frac{\Delta t}{A_i} \sum_{j \in N(i)} (\mathbf{F}_{i,j}^{n+1/2} n_{i,j}^{(x)} + \mathbf{G}_{i,j}^{n+1/2} n_{i,j}^{(y)}) w_{i,j} \tag{7}$$

where A_i is the area of the cell i, $\mathbf{F}_{i,j}^{n+1/2}$ and $\mathbf{G}_{i,j}^{n+1/2}$ are the average values between the time levels n and $n+1$ of **F** and **G** across the interface between the cells i and j, $N(i)$ is the set of the neighbour cells of i, $n_{i,j}^{(x)}$, $n_{i,j}^{(y)}$ are the x and y components of the normal unit vector of the interface (i, j) between the cells i and j, Δt is the computational time step and $w_{i,j}$ is the width of the interface (i, j). The normal unit vector $n_{i,j}$ is oriented from the cell i to the cell j.
(6) The source term **S** is incorporated to the solution. This can be done using time splitting [15] or by discretizing the source term directly at the time level n.

2. RECONSTRUCTION OF VARIABLES OVER UNSTRUCTURED GRIDS

2.1. The reconstruction process

The performance of Godunov-type schemes is largely conditioned by the reconstruction process to obtain $\widetilde{\mathbf{U}}_i^n(x, y)$, corresponding to the second step of Godunov-type schemes. In the original Godunov scheme [1] $\widetilde{\mathbf{U}}_i^n(x, y)$ is taken constant, equal to $\mathbf{U}_i^n$. In higher-order schemes, $\widetilde{\mathbf{U}}_i^n(x, y)$ is assumed to be a linear or higher-order function of space (see e.g. References [16, 17] for linear reconstructions on Cartesian grids and Reference [7] for linear reconstructions on triangular grids). The reconstructed profile considered here is a linear profile, i.e. a plane, leading to second-order

DOI: 10.1002/fld

spatial accuracy of the results. Second-order accuracy in time is then achieved through the time integration procedure.

The reconstructed profile over the cell i at the time level n, denoted by $\widetilde{\mathbf{U}}_i^n(x, y)$, must satisfy the following constraints:

(1) The average value of $\widetilde{\mathbf{U}}_i^n(x, y)$ over the cell i must be equal to the cell average $\mathbf{U}_i^n$ [4]

$$\frac{1}{A_i}\int_{\Omega_i} \widetilde{\mathbf{U}}_i^n(x, y)\,\mathrm{d}x\,\mathrm{d}y = \mathbf{U}_i^n \tag{8}$$

where Ω_i denotes the set of points of the cell i.

(2) The value of $\widetilde{\mathbf{U}}_i^n(x, y)$ at the centre (x_j, y_j) of the cells j neighbour to cell i should be as close as possible to the neighbour cell average

$$\widetilde{\mathbf{U}}_i^n(x_j, y_j) \cong \mathbf{U}_j^n \quad \forall j \in N(i) \tag{9}$$

where $N(i)$ denotes the set of cells neighbour to cell i.

Equations (8) and (9) yield $E_i + 1$ constraints on the function $\widetilde{\mathbf{U}}_i^n(x, y)$, where E_i is the number of neighbours of the cell i. This leads to four conditions for a triangular cell and to five conditions for a quadrangular cell. In most cases all these conditions cannot be satisfied simultaneously and residual minimisation procedures, such as least-square fitting, must be used to adjust the parameters of the reconstruction.

In classical MUSCL approach, this procedure, described in Section 2.2, is applied to each component of the conserved variable $\mathbf{U}$, thus to h, q_x and q_y. The way the classical MUSCL approach was adapted to unstructured grids is presented in Section 2.4. The proposed approach, presented in Section 3, allows a profile to be reconstructed for each of the conserved variables, while only based on the linear reconstruction of the water depth h.

2.2. Two-dimensional linear reconstruction

The principle of the two-dimensional linear reconstruction is given for a scalar variable U. When applied to a vector variable, the reconstruction must be carried out independently for each component of the vector variable. A two-dimensional linear reconstruction $\widetilde{U}_i^n$ of a given scalar variable U on a given cell i is sought. The cell may have any arbitrary number of edges. The reconstruction $\widetilde{U}_i^n$ of U in the cell i at the time level n takes the form

$$\widetilde{U}_i^n(x, y) = (x - x_i)a_i + (y - y_i)b_i + c_i \tag{10}$$

where x_i and y_i are the co-ordinates of the gravity centre of the cell i. The reconstructed profile $\widetilde{U}_i^n$ is determined from the known average value U_i^n of U on the cell at the time level n and from the known average values U_j^n in each of the neighbouring cells. It is now explained how to determine such a reconstructed profile $\widetilde{U}_i^n$ that satisfies constraints (8) and (9).

Substituting Equation (10) into Equation (8) leads to the following condition on c_i:

$$c_i = U_i^n \tag{11}$$

In order to determine the slopes of the linear profile over the cell, the closest plane to the known U_j^n is determined by minimizing the square of the distance between the known and reconstructed

DOI: 10.1002/fld

values. This is done by minimizing the total residual function R_i defined as

$$R_i(a_i, b_i) = \sum_{j \in N(i)} [\widetilde{U}_i^n(x_j, y_j) - U_j^n]^2 \tag{12}$$

where $N(i)$ is the set of cells neighbour to cell i. The optimal values of a_i and b_i are those for which the derivatives $\partial R_i/\partial a_i$ and $\partial R_i/\partial b_i$ are equal to zero. Substituting Equations (10)–(11) into Equation (12) and differentiating R_i with respect to a_i and b_i yields the following conditions:

$$\begin{aligned} &\sum_{j \in N(i)} (x_j - x_i)^2 a_i + (x_j - x_i)(y_j - y_i) b_i + (x_j - x_i)(U_i^n - U_j^n) = 0 \\ &\sum_{j \in N(i)} (x_j - x_i)(y_j - y_i) a_i + (y_j - y_i)^2 b_i + (y_j - y_i)(U_i^n - U_j^n) = 0 \end{aligned} \tag{13}$$

This 2×2 system can be easily solved for a_i and b_i.

2.3. Slope limiting

A slope limiting procedure is needed in order to ensure that the reconstructed profiles do not induce any undershoots or overshoots of the solution. Various limiters for the solution of one- or two-dimensional equations with different levels of complexity are available from the literature (see e.g. References [4–9]). The present slope limiter is adapted from the monotonized central-difference limiter of Van Leer [2, 6], stating that, in one-dimensional problems, the slope σ_i in cell i for a variable U is given by

$$\sigma_i^n = \text{minmod}\left(\frac{U_{i+1}^n - U_{i-1}^n}{2\Delta x}, \beta\frac{U_i^n - U_{i-1}^n}{\Delta x}, \beta\frac{U_{i+1}^n - U_i^n}{\Delta x}\right) \tag{14}$$

with $\beta = 2$. This method compares the central difference with twice the one-sided slope to either side.

In the present case, a linear profile is reconstructed over each cell in the unstructured grid (typically, triangular cells), as described in the previous section. This linear profile corresponds to a plane as close as possible to the average values in the neighbouring cells. It can thus be seen as a kind of central difference. The slopes of this reconstructed profile are then compared to the local slopes across each cell interface multiplied by a factor β, as is done in Equation (14). As suggested in Reference [7], it is chosen to avoid local extrema at the cell-edge midpoint rather than avoiding local extrema at the cell nodes in order to obtain a less restrictive limiter. The limiting procedure is detailed below.

To limit the slopes of the reconstructed profile in cell i, they are multiplied by a factor γ, with

$$0 \leqslant \gamma \leqslant 1 \tag{15}$$

Note that it is chosen to reduce the slopes in the x and y directions by the same factor because this keeps the direction of the slope vector unchanged. The factor γ is obtained as follows, for example when applying the limiting procedure to the reconstructed profile $\widetilde{U}_i$ in cell i, at the interface with

DOI: 10.1002/fld

cell j. The limiter factor $\gamma_{i,j}$ is calculated as

$$\gamma_{i,j}=\begin{cases}\beta\dfrac{U_{i,j}^{\min}-U_i^n}{\widetilde{U}_{i,j}^n-U_i^n} & \text{if } (\widetilde{U}_{i,j}^n-U_i^n)<\beta(U_{i,j}^{\min}-U_i^n)\\ \beta\dfrac{U_{i,j}^{\max}-U_i^n}{\widetilde{U}_{i,j}^n-U_i^n} & \text{if } (\widetilde{U}_{i,j}^n-U_i^n)>\beta(U_{i,j}^{\max}-U_i^n)\\ 1 & \text{otherwise}\end{cases} \tag{16}$$

where $U_{i,j}^{\min}=\min(U_i,U_j)$, $U_{i,j}^{\max}=\max(U_i,U_j)$, and $\widetilde{U}_{i,j}^n$ is the value extrapolated at the interface from the reconstructed profile $\widetilde{U}_i$. The coefficient β is set to 2 to recover the monotonized central-difference limiter. More generally, this coefficient can be used to relax ($\beta>1$) or constrain ($\beta<1$) the process, which will be useful when looking at the applications presented at the end of this paper.

2.4. The MUSCL scheme

The MUSCL approach is presented here as it was used for comparison with the proposed eigenvector-based scheme, detailed in the next section. It consists in an adaptation to unstructured grids of the scheme developed by Alcrudo and Garcia-Navarro [9] who introduced this high-resolution method for the two-dimensional shallow-water equations on structured grids. The key steps are recalled here.

The solution at time $n+1$ is obtained by a predictor–corrector sequence. The algorithm is the following.

(1) Reconstruct the vector variable $\mathbf{U}$ over the cells in the computational domain. This yields the reconstructed profiles $\widetilde{\mathbf{U}}_i^n(x,y)$ at the time level n, with discontinuities at each cell interface.

(2) At each interface (i,j) between the cells i and j, define and solve the following Riemann problem with left and right states $\mathbf{U}_\mathrm{L}$ and $\mathbf{U}_\mathrm{R}$ in the coordinate system normal to the interface (Figure 1) defined as

$$\mathbf{U}(\xi)=\begin{cases}\mathbf{U}_\mathrm{L}=\widetilde{\mathbf{U}}_i^n(\xi_{i,j}) & \text{for } \xi<\xi_{i,j}\\ \mathbf{U}_\mathrm{R}=\widetilde{\mathbf{U}}_j^n(\xi_{i,j}) & \text{for } \xi>\xi_{i,j}\end{cases} \tag{17}$$

where $\xi_{i,j}$ is the ξ coordinate of the interface. In the notation above, the cells i and j are located on the left- and right-hand sides of the interface, respectively. Solving the Riemann problem at the interface (i,j) yields the predictor fluxes $\mathbf{F}_{i,j}^{(P)}$ and $\mathbf{G}_{i,j}^{(P)}$ in the x and y directions, respectively.

(3) Use the predictor fluxes over half a time step to obtain updated values $\mathbf{U}_i^{n+1/2}$ of $\mathbf{U}$ over the cells

$$\mathbf{U}_i^{n+1/2}=\mathbf{U}_i^n-\frac{\Delta t}{2A_i}\sum_{j\in N(i)}(\mathbf{F}_{i,j}^{(P)}n_{i,j}^{(x)}+\mathbf{G}_{i,j}^{(P)}n_{i,j}^{(y)})w_{i,j} \tag{18}$$

DOI: 10.1002/fld

(4) At each interface (i, j) between the cells i and j, define and solve the Riemann problem using the updated values

$$\mathbf{U}(\xi) = \begin{cases} \mathbf{U}_{\mathrm{L}} = \tilde{\mathbf{U}}_i^{n+1/2} & \text{for } \xi < \xi_{i,j} \\ \mathbf{U}_{\mathrm{R}} = \tilde{\mathbf{U}}_j^{n+1/2} & \text{for } \xi > \xi_{i,j} \end{cases} \tag{19}$$

where the slopes of the reconstructed profiles $\tilde{\mathbf{U}}_i^{n+1/2}$ and $\tilde{\mathbf{U}}_j^{n+1/2}$ are taken equal to the slopes computed during step 1. Solving this Riemann problem at the interface (i, j) yields the corrector fluxes $\mathbf{F}_{i,j}^{(C)}$ and $\mathbf{G}_{i,j}^{(C)}$ in the x and y directions, respectively.

(5) Use the corrector fluxes to compute the final value of $\mathbf{U}$ at the time level $n+1$

$$\mathbf{U}_i^{n+1} = \mathbf{U}_i^n - \frac{\Delta t}{A_i} \sum_{j \in N(i)} (\mathbf{F}_{i,j}^{(C)} n_{i,j}^{(x)} + \mathbf{G}_{i,j}^{(C)} n_{i,j}^{(y)}) w_{i,j} \tag{20}$$

It should be noted that this procedure involves solving twice a Riemann problem per time step. In addition, the classical MUSCL reconstruction is carried out separately on each component of the vector variable $\mathbf{U}$. The proposed approach, in contrast, requires the Riemann problem to be solved only once and only one component of $\mathbf{U}$ to be reconstructed per time step.

3. THE EIGENVECTOR-BASED RECONSTRUCTION (EVR)

The EigenVector-based Reconstruction (EVR) approach can be seen as a variation of the common MUSCL [2, 4] approach to unstructured grids. This approach is inspired from the GRP method of Ben-Artzi and Falcovitz [10] and Colella and Woodward in their PPM method [3], but it makes advantageous use of the eigenstructure of the equations to reduce the computational effort. The proposed approach has been applied successfully to the solution of the one-dimensional equations for two-phase flow in pipes [11, 12] and the Saint-Venant equations [13, 14]. In the original GRP method, as well as in the EVR method, second-order accuracy is achieved by averaging the fluxes in time over the time step Δt. The motivation for developing the EVR approach was twofold: (i) in the particular case of the shallow-water equations, thanks to the eigenstructure of the equations, the reconstruction of only one flow variable (namely the water depth) is needed instead of three as in the classical MUSCL approach, and (ii) the classical MUSCL approach may yield stability problems near wetting or drying fronts when applied to the shallow-water equations (see Section 4). As shown in Appendix A, one of the reasons for this is that the original MUSCL approach uses independent reconstructions for the water depths and the unit discharges. The limiting process may therefore act independently on the water depth and on the unit discharge profiles. This has the particular consequence that very large (if not infinite) reconstructed velocities may be obtained in the neighbourhood of wetting or drying fronts. Reducing the computation time step may have the counter-intuitive effect of making the problem more acute, as shown in Appendix A. The analysis made in Appendix A leads to conclude that the unit discharges should not be reconstructed independently from the water depth near wetting and drying fronts. In the EVR approach, the reconstruction of the x and y unit discharges is derived directly from that of the water depth, avoiding in such a way the problem of independent reconstruction leading to artificially high velocities near the wetting front.

DOI: 10.1002/fld

3.1. Governing equations in the base of eigenvectors

Since the present subsection focuses on the solution of the hyperbolic part of Equation (1), the source term **S** will be omitted in what follows. The fluxes at each interface are computed by solving Equation (11) in the local co-ordinate system (ξ, ψ) attached to the interface (i, j). Therefore, use is made of the rotational invariance property of Equation (11), stating that (demonstration in Reference [4])

$$\cos\theta_\xi \mathbf{F}(\mathbf{U}) + \sin\theta_\xi \mathbf{G}(\mathbf{U}) = \mathbf{T}_\xi^{-1}\mathbf{F}(\mathbf{T}_\xi \mathbf{U}) \tag{21}$$

where ξ and ψ are the coordinates in the direction of the normal and tangent unit vector, respectively, making an angle θ_ξ with the x direction. Using Equation (21), following Reference [4], Equation (11) in the local co-ordinates system becomes the so-called augmented one-dimensional system

$$\frac{\partial \mathbf{V}}{\partial t} + \frac{\partial \mathbf{F}_\xi}{\partial \xi} = 0 \tag{22}$$

where $\mathbf{V} = \mathbf{T}_\xi \mathbf{U}$ and $\mathbf{F}_\xi = \mathbf{F}(\mathbf{T}_\xi \mathbf{U})$ are the transformed expressions of **U**, **F** and **G** in the local coordinate system.

The principle of the EVR method is the following. Equation (22) can be written in characteristic form as

$$\frac{\partial \mathbf{V}}{\partial t} + \mathbf{A}\frac{\partial \mathbf{V}}{\partial \xi} = 0 \tag{23}$$

where $\mathbf{A} = \partial \mathbf{F}_\xi / \partial \mathbf{V}$ is the Jacobian matrix of $\mathbf{F}_\xi$ with respect to **V**

$$\mathbf{A} = \begin{bmatrix} 0 & 1 & 0 \\ c^2 - u^2 & 2u & 0 \\ -uv & v & u \end{bmatrix} \tag{24}$$

where u and v are the velocity components in the directions normal and tangent to the interface, respectively. The matrix **A** has the following eigenvalues and associated right eigenvectors, denoted by $\lambda^{(p)}$ and $\mathbf{K}^{(p)}$, respectively. They satisfy the following equality:

$$\mathbf{A}\mathbf{K}^{(p)} = \lambda^{(p)}\mathbf{K}^{(p)} \tag{25}$$

Straightforward algebra leads to the following expressions for $\lambda^{(p)}$ and $\mathbf{K}^{(p)}$:

$$\lambda^{(1)} = u - c, \quad \lambda^{(2)} = u, \quad \lambda^{(3)} = u + c$$

$$\mathbf{K}^{(1)} = \begin{bmatrix} 1 \\ u - c \\ v \end{bmatrix}, \quad \mathbf{K}^{(2)} = \begin{bmatrix} 0 \\ 0 \\ 1 \end{bmatrix}, \quad \mathbf{K}^{(3)} = \begin{bmatrix} 1 \\ u + c \\ v \end{bmatrix} \tag{26}$$

The vector **V** is written as a combination of the eigenvectors of the characteristic matrix **A**:

$$\mathbf{V}(\xi, \psi, t) = \sum_p \alpha^{(p)}(\xi, \psi, t)\mathbf{K}^{(p)} = \mathbf{K}\boldsymbol{\alpha}(\xi, \psi, t) \tag{27}$$

DOI: 10.1002/fld

where $\alpha^{(p)}$ is the coefficient (called the *wave strength*) of the combination associated to the pth wave, $\mathbf{K}$ is the matrix formed by the eigenvectors $\mathbf{K}^{(p)}$ and $\boldsymbol{\alpha}$ is the vector formed by the wave strengths $\alpha^{(p)}$. Note that, given Equations (26) and (27), the wave strengths for the shallow-water equations are given by

$$\begin{aligned} \alpha^{(1)} &= h/2 \\ \alpha^{(2)} &= 0 \\ \alpha^{(3)} &= h/2 \end{aligned} \tag{28}$$

Substituting Equation (27) into Equation (24) yields

$$\frac{\partial}{\partial t}\mathbf{K}\boldsymbol{\alpha} + \mathbf{A}\frac{\partial}{\partial \xi}\mathbf{K}\boldsymbol{\alpha} = 0 \tag{29}$$

Left-multiplying Equation (29) by the matrix $\mathbf{K}^{-1}$ leads to

$$\mathbf{K}^{-1}\frac{\partial}{\partial t}\mathbf{K}\boldsymbol{\alpha} + \mathbf{K}^{-1}\mathbf{A}\frac{\partial}{\partial \xi}\mathbf{K}\boldsymbol{\alpha} = 0 \tag{30}$$

In the computational cell i, $\mathbf{A}$ is approximated by the constant matrix $\mathbf{A}_i^n$ and $\mathbf{K}$ is approximated by the constant matrix $\mathbf{K}_i^n$ that can thus be taken out of the differentiation operators to give

$$\mathbf{K}_i^{n^{-1}}\mathbf{K}_i^n\frac{\partial}{\partial t}\boldsymbol{\alpha} + \mathbf{K}_i^{n^{-1}}\mathbf{A}_i^n\mathbf{K}_i^n\frac{\partial}{\partial \xi}\boldsymbol{\alpha} = 0 \tag{31}$$

This approximation of the original vector equation is nothing but a local linearization of the problem in the cell i. Noticing that the matrix product $\mathbf{K}_i^{n^{-1}}\mathbf{A}_i^n\mathbf{K}_i^n$ is equal to the diagonal matrix $\boldsymbol{\Lambda}_i^n$ formed by the eigenvalues of $\mathbf{A}_i^n$, Equation (31) becomes

$$\frac{\partial \boldsymbol{\alpha}}{\partial t} + \boldsymbol{\Lambda}_i^n\frac{\partial \boldsymbol{\alpha}}{\partial \xi} = 0 \tag{32}$$

Equation (32) is equivalent to the following set of differential relationships:

$$\frac{\mathrm{d}\alpha^{(p)}}{\mathrm{d}t} = 0 \quad \text{along } \frac{\mathrm{d}\xi}{\mathrm{d}t} = \lambda_i^{(p),n} \tag{33}$$

where $\lambda_i^{(p),n}$ is the pth eigenvalue of $\mathbf{A}_i^n$.

Equations (33) that state the invariance of the wave strengths along the characteristic lines are called the compatibility equations along these characteristic lines.

3.2. Computation of the intercell fluxes

Assuming that linear reconstructed profiles $\widetilde{\mathbf{U}}_i$ are available in each cell, those form GRPs at each cell interface. The evolution in time of the cell average $\mathbf{U}_i^{n+1}$ is computed according to the balance equation (7), in which $\mathbf{F}_{i,j}^{n+1/2}$ and $\mathbf{G}_{i,j}^{n+1/2}$ are the average values of the x and y fluxes across the interface (i, j) between the time levels n and $n+1$. Considering a local co-ordinates system (ξ, ψ)

DOI: 10.1002/fld

attached to the interface (i, j), the flux to be computed across the interface is the flux $\mathbf{F}_{\eta,i,j}^{n+1/2}$ in the direction normal to the interface, according to Equation (24). In the original GRP method [10, 18] this numerical flux is defined as

$$\mathbf{F}_{\xi,i,j}^{n+1/2} = \int_{t^n}^{t^{n+1}} \int_{-w_{i,j}/2}^{w_{i,j}/2} \mathbf{V}_{i,j}(\xi, \psi, t)\, \mathrm{d}\psi\, \mathrm{d}t \approx \mathbf{F}(\mathbf{V}_{i,j}(0, 0, t^{n+1/2})) \tag{34}$$

where $w_{i,j}$ is the length of the interface and $\mathbf{V}_{i,j}(\xi, \psi, t)$ is the solution of the GRP between two reconstructed states $\widetilde{\mathbf{U}}_i$ and $\widetilde{\mathbf{U}}_j$ on the left and right side of the interface, respectively. The time-averaged flux is thus obtained from $\mathbf{V}_{i,j}(0, 0, t^{n+1/2})$ via a mid-point rule approximation. However, such a method implies to compute the exact solution of the GRP, which is complicated in practice.

The method proposed here is inspired from a modification of the GRP method. At each cell interface, the GRP are replaced by ERPs that are solved like any classical one-dimensional Riemann problem. In the present applications, a two rarefaction wave Riemann solver was used (see Reference [14] for a detailed description). The numerical fluxes are defined as

$$\mathbf{F}_{\xi,i,j}^{n+1/2} = \mathbf{F}(\mathbf{V}_{i,j}^{n+1/2}) \tag{35}$$

where $\mathbf{V}_{i,j}^{n+1/2}$ is the solution of the ERP between two constant, time-averaged, states $\mathbf{V}_{i,j,\mathrm{L}}^{n+1/2}$ and $\mathbf{V}_{i,j,\mathrm{R}}^{n+1/2}$ on the left and right side of the interface, respectively. How to define those constant states will be detailed in the next section.

It must be noted that numerical fluxes computed using Equations (34) or (35) by means of a time-averaged value $\mathbf{V}_{i,j}^{n+1/2}$ is an alternative to the predictor–corrector sequence used in the MUSCL approach to obtain a second-order accurate scheme. It has the advantage that it provides a time-averaged flux across the interface. Although this expression might seem complicated to evaluate in practice, it will be shown in the next sections that Equation (28) allows the calculations to be simplified to a large extent. The left and right constant states $\mathbf{V}_{i,j,\mathrm{L}}^{n+1/2}$ and $\mathbf{V}_{i,j,\mathrm{R}}^{n+1/2}$ are defined as

$$\begin{aligned}
\mathbf{V}_{i,j,\mathrm{L}}^{n+1/2} &= \frac{1}{w_{i,j}\Delta t} \int_{t^n}^{t^{n+1}} \int_{-w_{i,j}/2}^{w_{i,j}/2} \mathbf{V}_{i,j,\mathrm{L}}(0, \psi, t)\, \mathrm{d}\psi\, \mathrm{d}t \\
\mathbf{V}_{i,j,\mathrm{R}}^{n+1/2} &= \frac{1}{w_{i,j}\Delta t} \int_{t^n}^{t^{n+1}} \int_{-w_{i,j}/2}^{w_{i,j}/2} \mathbf{V}_{i,j,\mathrm{R}}(0, \psi, t)\, \mathrm{d}\psi\, \mathrm{d}t
\end{aligned} \tag{36}$$

Making use of Equation (36) and considering a local linear problem in each cell, in such a way that the eigenvectors $\mathbf{K}^{(p)}$ can be replaced by their (constant) averages $\mathbf{K}_i^{(p),n}$ and $\mathbf{K}_j^{(p),n}$ over the cells i and j, respectively, Equation (36) can be written as

$$\begin{aligned}
\mathbf{V}_{i,j,\mathrm{L}}^{n+1/2} &= \frac{1}{w_{i,j}\Delta t} \int_{t^n}^{t^{n+1}} \int_{-w_{i,j}/2}^{w_{i,j}/2} \sum_p \alpha_{i,j,\mathrm{L}}^{(p)}(0, \psi, t)\mathbf{K}_i^{(p),n}\, \mathrm{d}\psi\, \mathrm{d}t \\
\mathbf{V}_{i,j,\mathrm{R}}^{n+1/2} &= \frac{1}{w_{i,j}\Delta t} \int_{t^n}^{t^{n+1}} \int_{-w_{i,j}/2}^{w_{i,j}/2} \sum_p \alpha_{i,j,\mathrm{R}}^{(p)}(0, \psi, t)\mathbf{K}_j^{(p),n}\, \mathrm{d}\psi\, \mathrm{d}t
\end{aligned} \tag{37}$$

DOI: 10.1002/fld

The summation under the integrals in Equation (37) is split into two parts according to the sign of the eigenvalues $\lambda^{(p)}$. This yields, for the left state $\mathbf{V}_{i,j,\mathrm{L}}(0,\psi,t)$:

$$\mathbf{V}_{i,j,\mathrm{L}}(0,\psi,t)=\sum_{\lambda_i^{n(p)}\geqslant 0}\alpha_{i,j,\mathrm{L}}^{(p)}(0,\psi,t)\mathbf{K}_i^{(p),n}+\sum_{\lambda_i^{n(p)}<0}\alpha_{i,j,\mathrm{L}}^{(p)}(0,\psi,t)\mathbf{K}_i^{(p),n} \tag{38}$$

Making use of the invariance property expressed by Equation (33), the values of $\alpha_{i,j,\mathrm{L}}^{(p)}$ with positive eigenvalues at the interface at a time t are deduced from the reconstructed value at time level n by tracing the pth wave strength backward in time within the cell i:

$$\alpha_{i,j,\mathrm{L}}^{(p)}(0,\psi,t)=\tilde{\alpha}_i^{(p),n}(\xi^{(p)},\psi^{(p)})\quad\text{for }\lambda_i^{(p),n}\geqslant 0 \tag{39}$$

where $\lambda_i^{(p),n}$ is the value of the pth wave celerity over the cell i and $(\xi^{(p)},\psi^{(p)})$ are the coordinates of the foot of the pth characteristic line issued from the midpoint of the interface (i,j) at time t:

$$\begin{aligned}\xi^{(p)}&=\xi-(t-t^n)\lambda_i^{(p),n}\\ \psi^{(p)}&=\psi\end{aligned} \tag{40}$$

The foot of this characteristics should be located within cell i to ensure the stability of the reconstruction. This condition is fulfilled if the time step is small enough to comply with the following CFL stability condition: the computational time step must be chosen such that the area of the domain of dependence of each interface of a given computational cell is smaller than or equal to the area of the cell (see Appendix B for a stability analysis).

From Equation (39), averaging the wave strength in time over the interface (i,j) as done in Equation (37) is equivalent to an averaging over the domain of dependence of the interface (Figure 2).

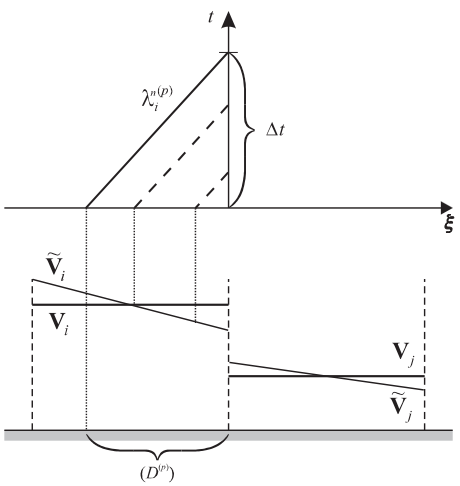

Figure 2. Construction of the left side of the ERP: equivalence of the average in time over Δt and the average over the domain of dependence $(D^{(p)})$.

DOI: 10.1002/fld

This average value of $\alpha_{i,j,\mathrm{L}}^{(p)}$ is denoted by $\alpha_{i,j,\mathrm{L}}^{(p),n+1/2}$ and is evaluated as

$$\alpha_{i,j,\mathrm{L}}^{(p)n+1/2} = \frac{1}{D^{(p)}} \int_{(D^{(p)})} \widetilde{\alpha}_i^{(p),n}(\xi,\psi)\,\mathrm{d}\xi\,\mathrm{d}\psi \quad \text{for } \lambda_i^{(p),n} \geqslant 0 \tag{41}$$

where $D^{(p)}$ is the area of the domain of dependence ($D^{(p)}$) of the interface for the pth wave. Expression (41) is valid for the wave strengths with positive eigenvalues, as they travel towards the interface and thus influence the solution at the interface. Since the wave strengths with negative eigenvalues travel in the direction opposite to the interface they do not influence the solution. Therefore, they can be taken equal to any arbitrary value. The simplest possible solution is to use the cell average

$$\alpha_{i,j,\mathrm{L}}^{(p)}(0,\psi,t) = \alpha_i^{(p),n} \quad \text{for } \lambda_i^{(p),n} < 0 \tag{42}$$

From Equations (41) and (42), $\alpha_{i,j,\mathrm{L}}^{(p),n+1/2}$ is given by

$$\alpha_{i,j,\mathrm{L}}^{(p),n+1/2} = \begin{cases} \dfrac{1}{D^{(p)}} \displaystyle\int_{(D^{(p)})} \widetilde{\alpha}_i^{(p),n}(\xi,\psi)\,\mathrm{d}\xi\,\mathrm{d}\psi & \text{if } \lambda_i^{(p),n} \geqslant 0 \\ \alpha_i^{(p),n} & \text{if } \lambda_i^{(p),n} < 0 \end{cases} \tag{43}$$

Reasoning by symmetry for the right-hand side of the interface leads to the following relationships:

$$\alpha_{i,j,\mathrm{R}}^{(p),n+1/2} = \begin{cases} \dfrac{1}{D^{(p)}} \displaystyle\int_{(D^{(p)})} \widetilde{\alpha}_j^{(p),n}(\xi,\psi)\,\mathrm{d}\xi\,\mathrm{d}\psi & \text{if } \lambda_j^{(p),n} \leqslant 0 \\ \alpha_j^{(p),n} & \text{if } \lambda_j^{(p),n} > 0 \end{cases} \tag{44}$$

3.3. A particular case: the linear reconstruction

In the case of a linear reconstruction, the integral in Equation (43) can be evaluated as

$$\alpha_{i,j,\mathrm{L}}^{(p),n+1/2} = \widetilde{\alpha}_i^{(p),n}(\xi_{\mathrm{C}},\psi_{\mathrm{C}}) \tag{45}$$

where the point C $(\xi_{\mathrm{C}},\psi_{\mathrm{C}})$ denotes the centre of the domain of dependence of the characteristic $\mathrm{d}\xi/\mathrm{d}t = \lambda_i^{(p),n}$, expressed in the local coordinate system (Figure 3). The coordinates of the point C are thus given by

$$\begin{aligned} \xi_{\mathrm{C}} &= -\lambda_i^{(p),n}\Delta t/2 \\ \psi_{\mathrm{C}} &= 0 \end{aligned} \tag{46}$$

For the shallow-water equations, Equation (28) shows that reconstructing only the water depths $\tilde{h}_i^n$ and $\tilde{h}_j^n$ allows the left and right states of the ERP to be determined completely.

Finally, according to (37) and making use of (31) and (38), the following expression is obtained for the left and right states of the ERP:

$$\begin{aligned} \mathbf{V}_{i,j,\mathrm{L}}^{n+1/2} &= \alpha_{i,j,\mathrm{L}}^{(1),n+1/2}\mathbf{K}_i^{(1),n} + \alpha_{i,j,\mathrm{L}}^{(3),n+1/2}\mathbf{K}_i^{(3),n} \\ \mathbf{V}_{i,j,\mathrm{R}}^{n+1/2} &= \alpha_{i,j,\mathrm{R}}^{(1),n+1/2}\mathbf{K}_j^{n(1)} + \alpha_{i,j,\mathrm{R}}^{(3),n+1/2}\mathbf{K}_j^{(3),n} \end{aligned} \tag{47}$$

DOI: 10.1002/fld

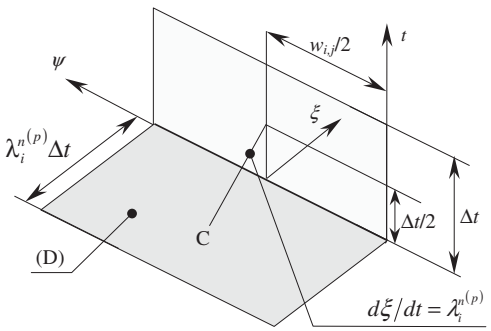

Figure 3. Equivalence between the average of a variable in time (light shaded region) and the average in space over the domain of dependence (dark shaded region).

3.4. Overview of the algorithm

The algorithm for the EVR reconstruction can be presented in a form similar to the MUSCL algorithm in Section 2.4.

(1) Reconstruct the wave strengths over the cells in the computational domain. Note that in the particular case of the shallow-water equations, only the water depth needs to be reconstructed. The reconstruction yields the profiles $\tilde{h}_i^n(x, y)$ at the time level n.
(2) At each interface (i, j) between the cells i and j, define and solve the Riemann problem given by Equations (47) in the coordinate system normal to the interface. Solving the Riemann problem at the interface (i, j) yields the fluxes $\mathbf{F}_{i,j}^{n+1/2}$ and $\mathbf{G}_{i,j}^{n+1/2}$ in the x and y directions, respectively. Note that in the case of a linear reconstruction the wave strengths in Equations (47) are obtained using Equations (45)–(46).
(3) Use the fluxes to compute the final value of $\mathbf{U}$ at the time level $n + 1$ according to Equation (7).

4. APPLICATION EXAMPLES

The performance of the EVR method is illustrated by two test cases, where the proposed reconstruction method is compared to the first-order Godunov scheme and to the classical MUSCL approach. In these examples, a two-rarefaction wave solver was used to compute the fluxes [14]. This solver is based on the fact that the Riemann invariants are a second-order approximation of the jump relationship in terms of the variable jump across a discontinuity [19]. Therefore, the Riemann invariants may be used as a reasonable approximation of the Rankine–Hugoniot conditions in the computation of approximate solutions of the Riemann problem. This Riemann-invariants-based scheme has proven its validity in a number of applications including gas dynamics [20, 21] and pipe flow simulations [22, 23].

The first test consists of a circular dam-break flow on a flat bottom, with different ratios between the initial water depths inside and outside the reservoir. For this test, a pseudo-analytical solution can be calculated [5]. The second test case shows a dam-break flow in a channel with a 90° bend, for which experimental measurements are available [24–26].

DOI: 10.1002/fld

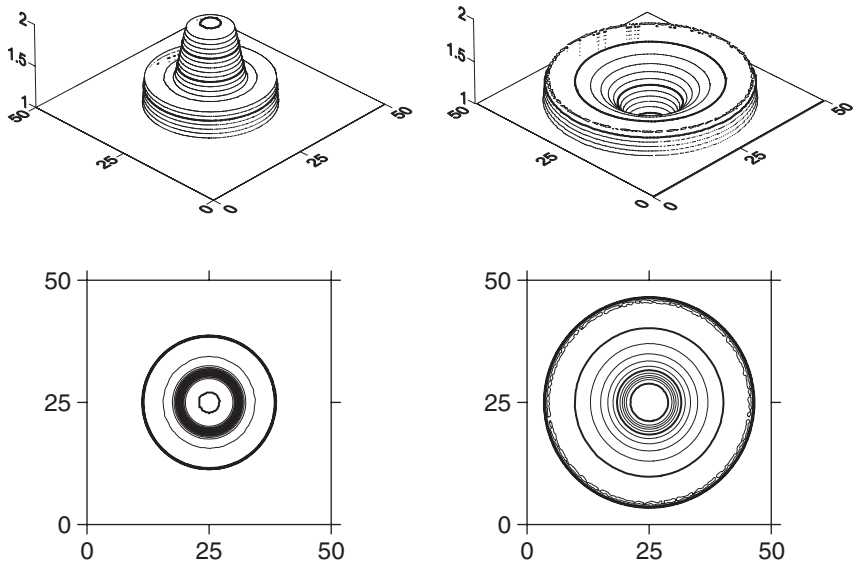

Figure 4. Perspective (top) and plan view (bottom) of the solution of the circular dam-break problem computed at $t = 1$ s (left) and $t = 3$ s (right) using a grid with 130 000 cells. Contour line spacing: 5 cm.

4.1. Circular dam break

This example consists of the instantaneous breaking of a cylindrical tank (diameter 20 m) initially filled with 2 m of water at rest. The wave generated by the breaking of the tank propagates into still water with an initial depth of (i) 1, (ii) 0.5, and (iii) 0 m (dry bed). Figure 4 illustrates this wave propagation over an initial water depth of 1 m by means of computations on a very fine mesh of 130 000 elements using the Godunov method. The numerical solution being identical to the theoretical solution obtained from the solution of the shallow-water equations expressed in a radial co-ordinate system [5], it can be considered as converged.

$$\begin{aligned} \frac{\partial h}{\partial t} + \frac{\partial}{\partial r}(hv_r) &= -\frac{hv_r}{r} \\ \frac{\partial v_r}{\partial t} + \frac{\partial}{\partial r}\left(hv_r^2 + \frac{1}{2}gh^2\right) &= -\frac{hv_r^2}{r} \end{aligned} \tag{48}$$

where v_r is the radial velocity, computed on a fine mesh of 2000 elements.

Figures 5–7 show results computed on a triangular mesh of 5024 cells, using the first-order Godunov scheme, the common MUSCL scheme and the EVR approach. Figure 5 compares the results for the propagation over an initial water depth of 1 m outside the reservoir. All computations were run on the same grid, with a maximum CFL number of 0.9 and, for the EVR and MUSCL schemes, a slope limiting coefficient $\beta = 2$. The Godunov scheme excessively smears the results, while both the EVR and the MUSCL scheme significantly improve the quality of the results. This is particularly clear in Figure 5(b): the water depth in the initial reservoir has dropped much lower

DOI: 10.1002/fld

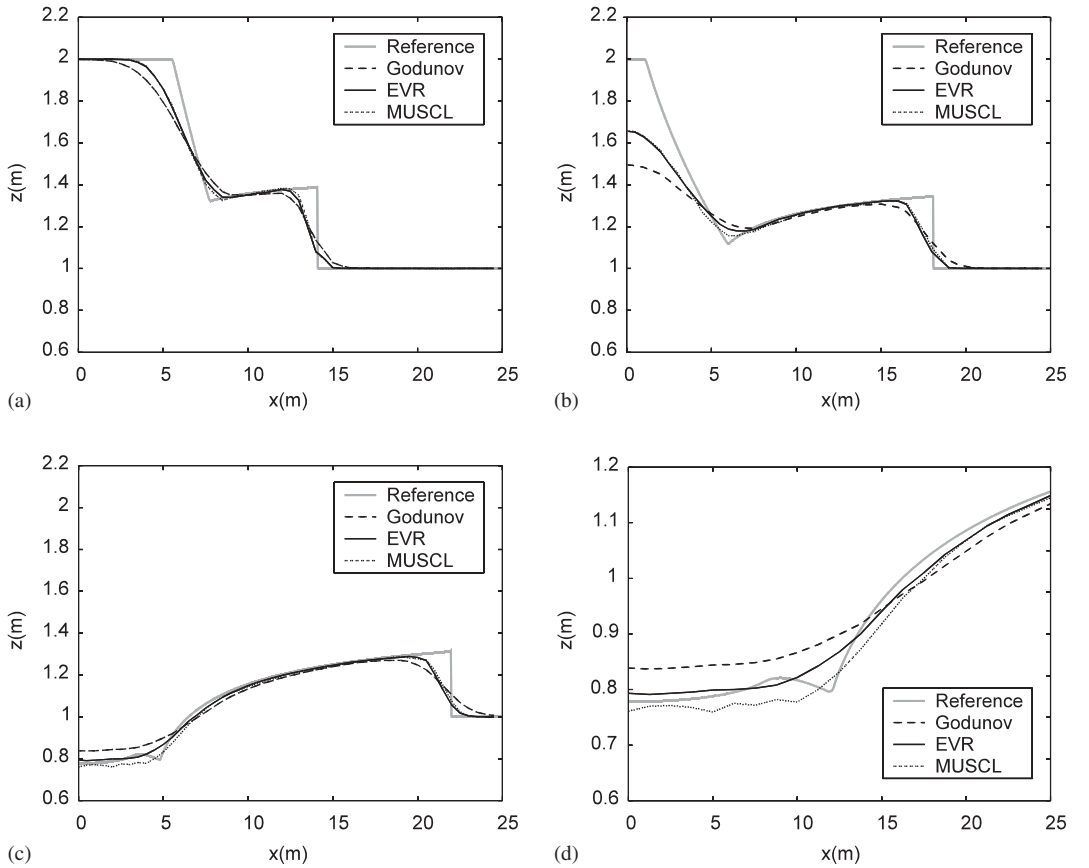

Figure 5. Comparison of numerical and semi-analytical results for the depth ratio 2 m/1 m at times: (a) 1; (b) 2; (c) 3 s; and (d) zoom on the results after 3 s.

with the Godunov scheme than with both higher-order methods. Looking at Figures 5(c) and (d), small oscillations appear in the MUSCL computations.

The results presented in Figure 6 correspond to an initial water depth of 0.5 m outside the reservoir. Again, all computations were run on the same grid of 5024 triangular cells, with a maximum CFL number of 0.9 and, for the EVR and MUSCL schemes, a coefficient β in the limiter equal to 2. The general trend is the same as in Figure 5. Both the EVR and the MUSCL scheme significantly improve the quality of the results, and small oscillations are observed with the MUSCL scheme.

Finally, the propagation over an initially dry bed was tested, and the results are presented in Figure 7. Using the same parameters as in the previous computations (CFL 0.9 and $\beta = 2$), the MUSCL approach failed as illustrated in Figure 7(a). To obtain stable results, it was necessary to restrain the maximum CFL number to 0.5 and the limiter factor β to 1. However, such restrictions were not needed for the EVR method. Figures 7(b)–(d) thus present results computed with

DOI: 10.1002/fld

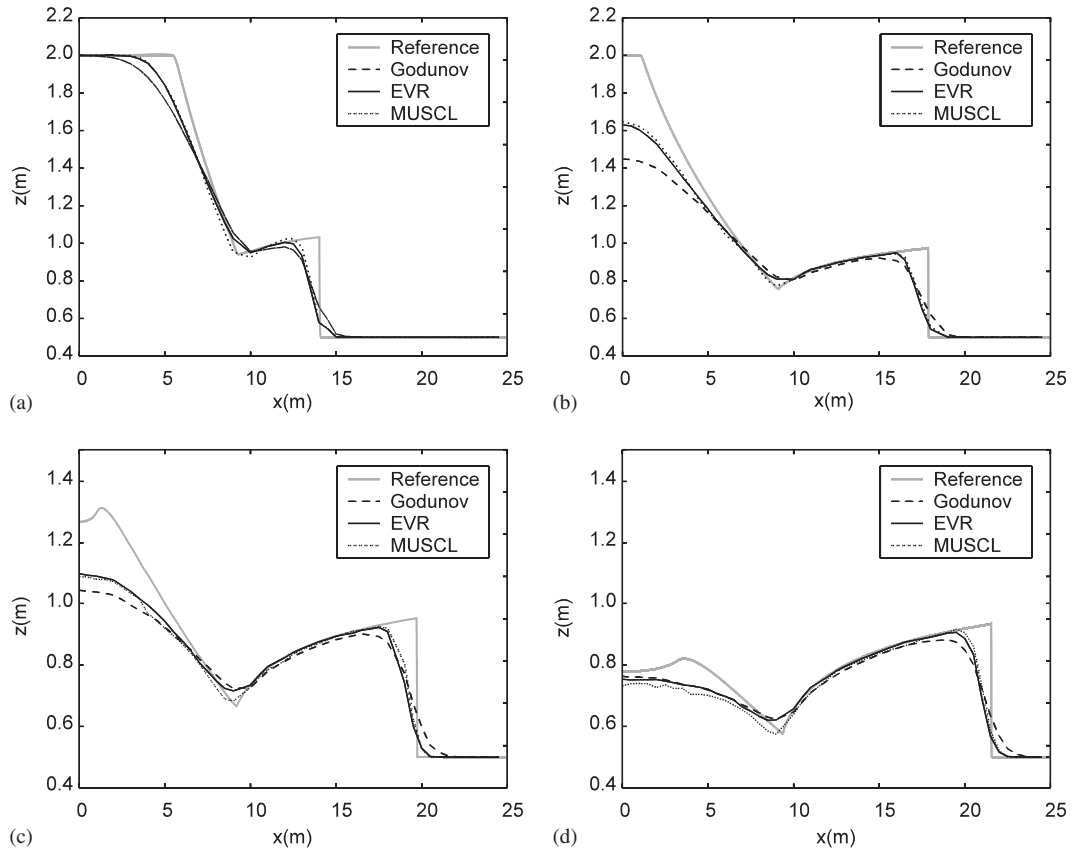

Figure 6. Comparison of numerical and semi-analytical results for the depth ratio 2 m/0.5 m at times: (a) 1; (b) 2; (c) 2.5; and (d) 3 s.

the Godunov scheme (CFL 0.9), the EVR method (CFL 0.9 and $\beta = 2$) and MUSCL (CFL 0.5 and $\beta = 1$).

Table I summarizes the computational time needed by each method for the series of test cases. The Godunov method, where no reconstruction is needed, is of course the faster of the three methods. Among the second-order schemes, the EVR method uses significantly less computational time as the MUSCL method. It can also be observed that the MUSCL approach is very slow in the dry bed case. This is partly due to the fact that the maximum CFL number had to be reduced to 0.5 instead of 0.9 in order to avoid instabilities. This is also due to the intrinsic difficulties attached to the MUSCL approach in the presence of dry beds, as explained in Appendix A.

4.2. Channel with a 90° *bend*

This example consists of a dam-break flow in an initially dry channel with a 90° bend. The experiments were carried out at the Civil Engineering Department of the Université catholique de

DOI: 10.1002/fld

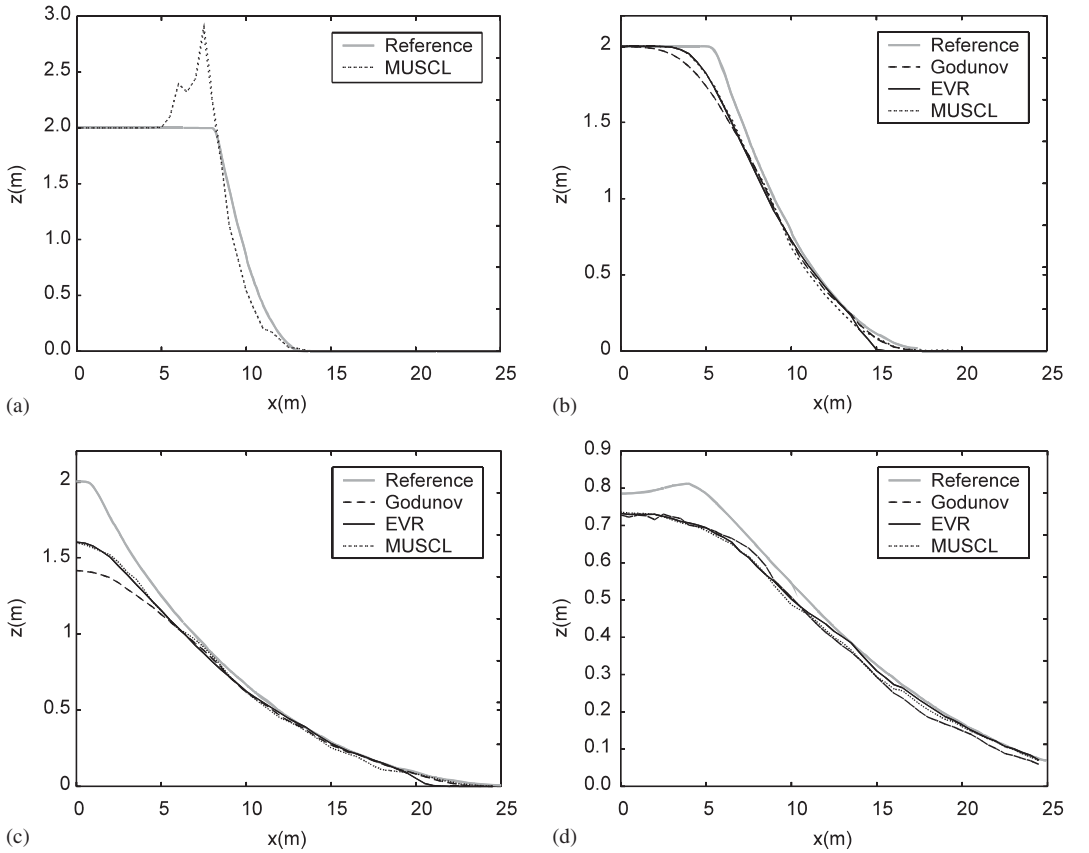

Figure 7. Comparison of numerical and semi-analytical results for the depth ratio 2 m/0 m: (a) failure of the MUSCL approach at 0.4 s; (b) results at 1 s, with the stabilized MUSCL scheme ($\beta = 1$ and CFL number of 0.5); (c) same results at 2 s; and (d) at 3 s.

Table I. Summary of computational times for the circular dam-break test cases, with an initial water depth in the tank of 2 m.

	Depth of the surrounding water (m)		
Approach	1	0.5	0 (dry bed)
Godunov	3.02	3.9	3.36
MUSCL	7.69	8.4	31.8
EVR	5.43	5.82	5.39

Louvain (UCL) in Belgium [24–26]. Figure 8 shows the configuration of the test case. The bed level in the reservoir is 0.33 m lower than the bed level in the channel, inducing an important step at the location of the dam. The initial water level in the reservoir is 0.25 m above the channel bed,

DOI: 10.1002/fld

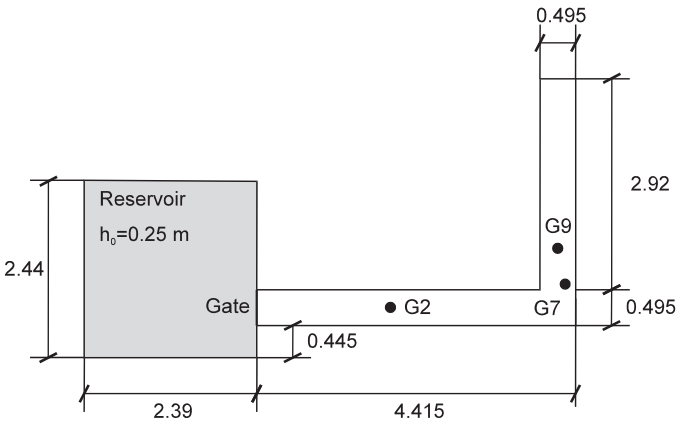

Figure 8. Definition sketch for the channel with a 90° bend test case and location of the gauges. Dimensions in metres.

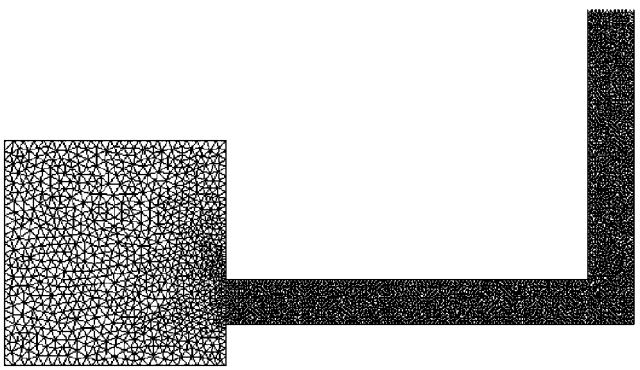

Figure 9. Mesh used for the computations of the 90° bend test case: 6888 triangular elements, with a greater density of triangles in the channel than in the reservoir.

and there is no water in the channel (dry bed). The Manning friction coefficient for the channel bed was estimated as $n_M = 0.013$. Figure 9 shows the 6888 element computational grid used for the simulations.

When the supercritical flow induced by the dam break reflects against the bend, its velocity becomes zero and the water level rises. Then, this water column collapses and a new water front propagates both in the downstream and upstream reaches. This results in a bore receding to the reservoir, with the consequence that the flow at the head of the bore becomes subcritical, and thus much slower than the initial supercritical flow. While the flow is mainly one-dimensional in the upstream part of the channel, it clearly features two-dimensional wave propagation in the downstream part, with cross-reflections against the channel side walls. This is illustrated in Figure 10, showing computed results after 6 s, using the EVR method.

DOI: 10.1002/fld

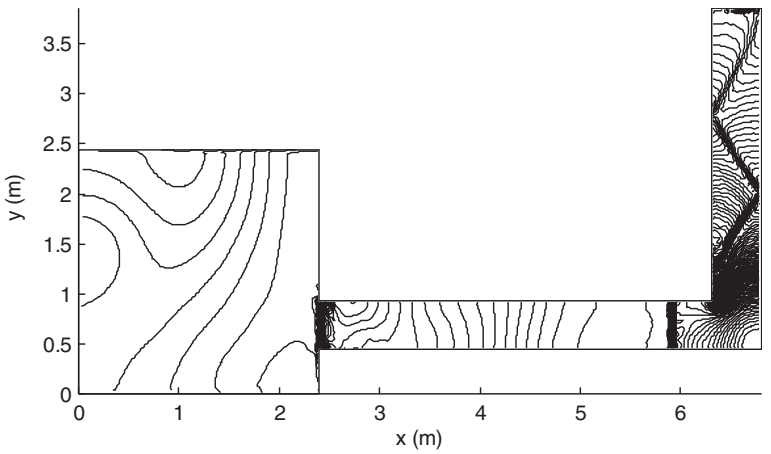

Figure 10. Structure of the flow after 6 s, computed with the EVR method. Contour line spacing 0.002 m.

For the computations using the original MUSCL scheme, it was again needed to reduce the maximum CFL number to 0.5 to avoid oscillations and instability, and to use $\beta = 1$, while for the Godunov method, the maximum CFL number was set to 0.9 and for the EVR method, the conditions were a CFL number of 0.9 and $\beta = 2$. Figure 11 shows the two-dimensional cross-waves in the downstream part of the channel after 6 s. The contour lines spacing is 0.002 m. Quite expectedly, the EVR and the MUSCL scheme yield a better resolution of the waves than does the Godunov method.

Comparisons with the experimental measurements a three different locations are presented in Figure 12, where the curves show the time evolution of the water depth. Note that all numerical methods give results very close to each other, except for the Godunov method at some locations. Figure 12(a) corresponds to a gauge located in the upstream reach. The arrival of the bore issued from the reflection of the water against the bend is clearly visible at $t = 10$ s. This arrival time is slightly delayed in the computations. The global agreement of the computed results with the experiments is good, but no method is able to reproduce all the undulations of free-surface recorded by the gauges. Possible sources of differences between the models and the experiments can be found in inaccuracies in the measurements (although the high reprodcibility of the measurements was demonstrated in Reference [26]) or inaccuracies in the Manning formula used to express the bottom friction, as this formula, widely used in the shallow-water framework, was initially derived for uniform-flow conditions. Moreover, the depth-averaged equations assume a hydrostatic pressure distribution, which is certainly not the case in the very first instants after the opening of the gate, and at the moment when the water strongly reflects in the bend. Also, viscosity and turbulent exchanges are neglected in the equations, which is a common assumption for rapid transient flows, but could explain some discrepancies. Figure 12(b) shows the results at a gauge located immediately downstream from the bend and Figure 12(c) shows the results in the downstream reach. All methods overestimate the water depth there, but this is rather due to the presence of cross-waves in the downstream reach: if the position of a wave is slightly shifted in the upstream or downstream direction by the numerical models, this may result in an important difference between the computed and measured water level at a gauging point.

DOI: 10.1002/fld

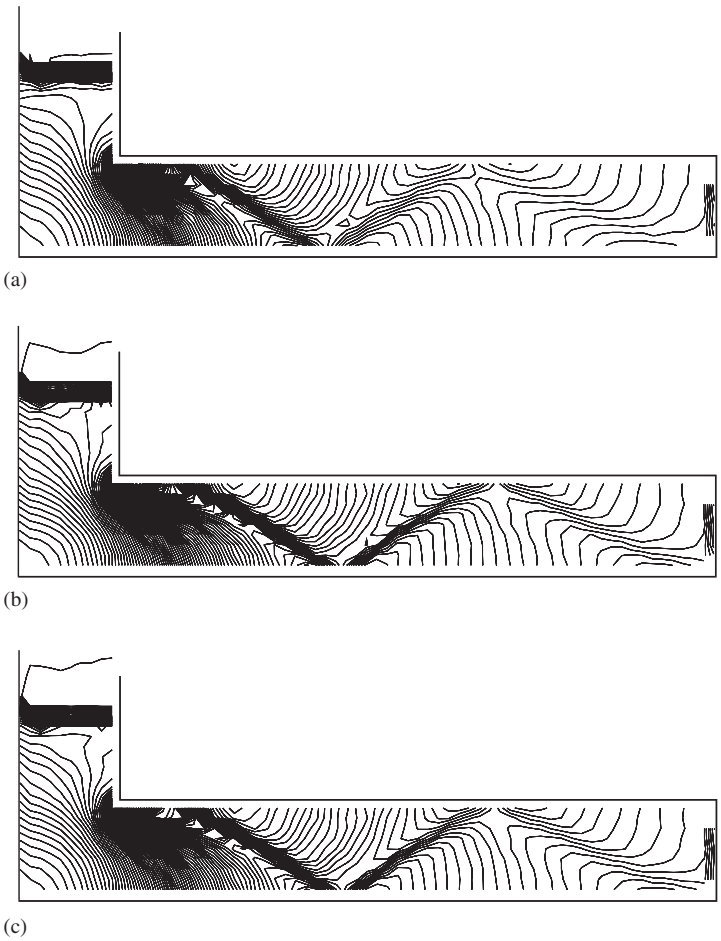

Figure 11. Two-dimensional cross-waves in the downstream part of the channel after 6 s computed with (a) the Godunov method; (b) EVR; and (c) MUSCL scheme. Contour line spacing 0.002 m.

Finally, a summary of the computational times is given in Table II. The EVR method again shows a significantly lower computational cost than the MUSCL scheme.

5. CONCLUSIONS

A new eigenvector-based reconstruction scheme to obtain second-order accuracy in the resolution of the shallow-water equations was presented. Taking advantage of the eigenstructure of this non-linear system of PDEs, the proposed method achieves a similar level of accuracy as the classical MUSCL approach, at a much lower computational cost. Besides, it is stable even near wetting and drying fronts, where the MUSCL approach shows some stability problems.

DOI: 10.1002/fld

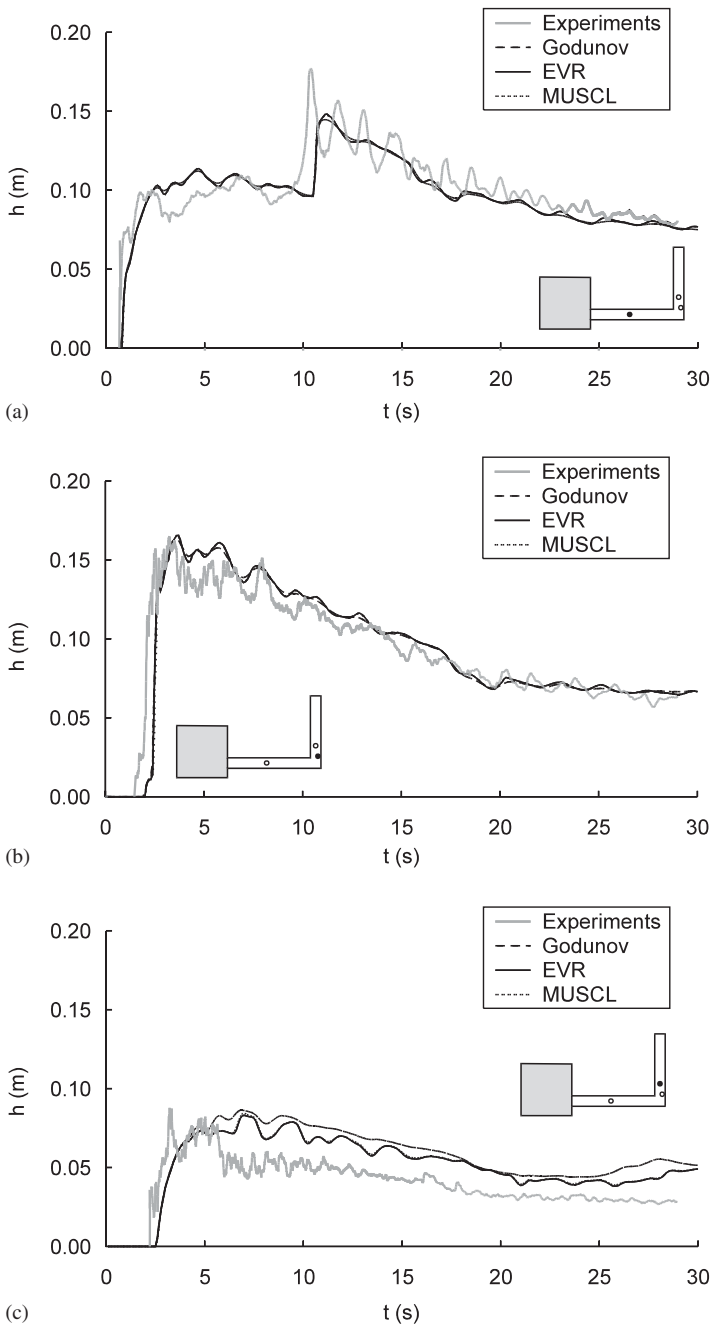

Figure 12. Comparison of experimental and numerical results at three gauging points: (a) Gauge No. 2 in the upstream reach; (b) Gauge No. 7 immediately downstream from the bend; and (c) Gauge No. 9 in the downstream reach.

DOI: 10.1002/fld

Table II. Summary of computational time for the 90° bend test case.

Approach	Normalized CPU time
Godunov	435.56
MUSCL	1169.15
EVR	646.31

The performance of the EVR method for the shallow-water equations was successfully assessed by two different types of test cases where the computational solution was compared to a semi-analytical solution and experimental measurements. The method could be extended to more general systems of hyperbolic equations, for which the MUSCL scheme is used to obtain higher-order accuracy.

APPENDIX A: OSCILLATORY CHARACTER OF THE ORIGINAL MUSCL RECONSTRUCTION NEAR WETTING FRONTS

The purpose of the present appendix is to demonstrate the possible oscillatory character of the original MUSCL reconstruction when applied to the shallow-water equations in the presence of wetting fronts. The classical dam break test case on a dry bed is considered. The dam break problem on a dry bed is defined as the following one-dimensional initial-value problem:

$$h(x,0)=\begin{cases} h_{\mathrm{L}} & \text{for } x<x_0 \\ 0 & \text{for } x>x_0 \end{cases} \qquad q(x,0)=0 \tag{A1}$$

The analytical solution of this problem is well-known [27]

$$h(x,t)=\begin{cases} h_{\mathrm{L}} & \text{for } \dfrac{x}{t}<-c_{\mathrm{L}} \\ \dfrac{1}{9g}\left(2c_{\mathrm{L}}-\dfrac{x}{t}\right)^2 & \text{for } -c_{\mathrm{L}}<\dfrac{x}{t}<2c_{\mathrm{L}} \\ 0 & \text{for } \dfrac{x}{t}>2c_{\mathrm{L}} \end{cases} \tag{A2a}$$

$$u(x,t)=\begin{cases} 0 & \text{for } \dfrac{x}{t}<-c_{\mathrm{L}} \\ \dfrac{2}{3}\left(c_{\mathrm{L}}+\dfrac{x}{t}\right) & \text{for } -c_{\mathrm{L}}<\dfrac{x}{t}<2c_{\mathrm{L}} \\ 0 & \text{for } \dfrac{x}{t}>2c_{\mathrm{L}} \end{cases} \tag{A2b}$$

where $c_{\mathrm{L}}=(gh_{\mathrm{L}})^{1/2}$ is the celerity of the pressure waves on the left-hand side of the initial discontinuity.

DOI: 10.1002/fld

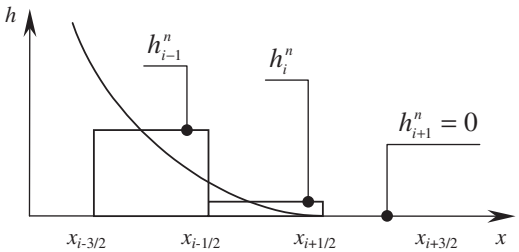

Figure A1. Dambreak problem on an initially dry bed. Discretization of the analytical solution in the neighbourhood of the wetting front.

Assume that profile (A2) is used as an initial condition for the MUSCL reconstruction. The x coordinate is discretized using a constant cell size Δx, in such a way that the wetting front, that moves at a speed $2c_{\mathrm{L}}$, is located at the interface $i + 1/2$ between the cells i and $i + 1$ (Figure A1). Then the abscissas of the cell interfaces are given by

$$\begin{aligned} x_{i-3/2} &= 2c_{\mathrm{L}}t^n - 2\Delta x \\ x_{i-1/2} &= 2c_{\mathrm{L}}t^n - \Delta x \\ x_{i+1/2} &= 2c_{\mathrm{L}}t^n \\ x_{i-3/2} &= 2c_{\mathrm{L}}t^n + \Delta x \end{aligned} \tag{A3}$$

where $x_{i-1/2}$ denotes the interface between the cells $i-1$ and i. Keeping in mind that the average values of h and $q_x = hu$ over the cells $i-1$, i and $i+1$ are defined as

$$h_i^n = \frac{1}{\Delta x}\int_{x_{i-1/2}}^{x_{i+1/2}} h(x, t^n)\,\mathrm{d}x \tag{A4a}$$

$$q_i^n = \frac{1}{\Delta x}\int_{x_{i-1/2}}^{x_{i+1/2}} hu(x, t^n)\,\mathrm{d}x \tag{A4b}$$

Substituting Equations (A2a) and (A3) into Equation (A4a) gives

$$\begin{aligned} h_{i-1}^n &= \frac{7}{27g}\left(\frac{\Delta x}{t^n}\right)^2 \\ h_i^n &= \frac{1}{27g}\left(\frac{\Delta x}{t^n}\right)^2 \\ h_{i+1}^n &= 0 \end{aligned} \tag{A5}$$

DOI: 10.1002/fld

Substituting Equations (A2) and (A3) into Equation (A4b) gives

$$\begin{aligned} q_{i-1}^n &= \frac{28c_{\mathrm{L}} - 15(\Delta x/t^n)}{54g}\left(\frac{\Delta x}{t^n}\right)^2 \\ q_i^n &= \frac{4c_{\mathrm{L}} - (\Delta x/t^n)}{54g}\left(\frac{\Delta x}{t^n}\right)^2 \\ q_{i+1}^n &= 0 \end{aligned} \tag{A6}$$

Applying the MUSCL reconstruction over the cell i leads to the following reconstructed profiles:

$$\begin{aligned} \tilde{h}_i^n(x) &= h_i^n + (x - x_i)h_{x_i}^n \\ \tilde{q}_i^n(x) &= q_i^n + (x - x_i)q_{x_i}^n \end{aligned} \tag{A7}$$

where $h_{x_i}^n$ and $q_{x_i}^n$ are the x slopes of the reconstructed profiles for h and q over the cell i and x_i is the x coordinate of the centre of the cell. In the original MUSCL procedure, $h_{x_i}^n$ and $q_{x_i}^n$ are first estimated as

$$\begin{aligned} h_{x_i}^n &\approx \frac{h_{i+1}^n - h_{i-1}^n}{2\Delta x} \\ q_{x_i}^n &\approx \frac{q_{i+1}^n - q_{i-1}^n}{2\Delta x} \end{aligned} \tag{A8}$$

and limited if necessary in such a way that no overshoot or undershoot of the average values over the cells $i-1$ and $i+1$ occurs in the reconstructed profiles. Substituting Equations (A5), (A6) and (A8) into Equation (A7) yields

$$\tilde{h}_i^n(x) = \left(1 - 7\frac{x - x_i}{2}\right)\frac{1}{27g}\left(\frac{\Delta x}{t^n}\right)^2 \tag{A9a}$$

$$\tilde{q}_i^n(x) = \left[4c_{\mathrm{L}} - \frac{\Delta x}{t} - \frac{x - x_i}{2\Delta x}\left(28c_{\mathrm{L}} - 15\frac{\Delta x}{t}\right)\right]\frac{1}{54g}\left(\frac{\Delta x}{t^n}\right)^2 \tag{A9b}$$

For $x = x_{i+1/2} = x_i + \Delta x/2$, Equation (A9a) leads to a negative value of h, which indicates that slope limiting is needed. The slope limiting process leads to redefining $h_{x_i}^n$ as

$$h_{x_i}^n \approx \frac{2}{27g}\left(\frac{\Delta x}{t^n}\right)^2 \tag{A10}$$

With this definition of $h_{x_i}^n$, Equation (A7) leads to the following value of h for $x = x_{i+1/2}$:

$$\tilde{h}_i^n(x_{i+1/2}) = 0 \tag{A11}$$

Equation (A9b) leads to the following value of q for $x = x_{i+1/2}$:

$$\tilde{q}_i^n(x_{i+1/2}) = \left(-12c_{\mathrm{L}} + 11\frac{\Delta x}{t^n}\right)\frac{1}{216g}\left(\frac{\Delta x}{t^n}\right)^2 \tag{A12}$$

DOI: 10.1002/fld

$\tilde{q}_i^n(x_{i+1/2})$ is strictly positive provided that

$$\Delta x > \frac{12}{11} c_L t^n \tag{A13}$$

This condition is verified at early simulation times, where t^n is sufficiently small. This has the consequence that if small time steps are used, the reconstructed q profile does not need to be limited at the beginning of the simulation, while the reconstructed h profile does. Therefore, the reconstructed unit discharge is non-zero in the neighbourhood of the interface $i+1/2$, while the reconstructed water depth is. This leads to an infinite reconstructed velocity at the interface $i+1/2$ that materializes the location of the wetting front. Reducing the computational time step leads to reducing the size of the domain of dependence of the interface $i+1/2$ and yields a larger value of the average velocity. The momentum flux from the cell i to the cell $i+1$ is grossly overestimated, leading to oscillations in the neighbourhood of the front. Given the non-linear character of the shallow-water equations, repeating the process a sufficient number of times may lead to instabilities in the numerical solution. It is not argued that the present analysis covers all the possible causes for instability in free-surface flow simulations. However, it provides a plausible explanation for the numerical problems arising near wetting and drying fronts. The present analysis allows the following recommendations to be drawn: (i) in the neighbourhood of wetting fronts, perform a reconstruction on the unit discharge only and reconstruct the water levels using the (constant) average value over the cell, or (ii) use constant reconstructions for both the water depth and the unit discharge in the neighbourhood of wetting fronts, or (iii) reconstruct only the water depth and use it as a basis for the reconstruction of the unit discharge everywhere in the model. The reconstruction method proposed in the present paper follows this third line.

APPENDIX B: STABILITY ANALYSIS

The purpose of the present appendix is to provide a justification to the CFL stability condition on unstructured triangular grids when an explicit scheme is used. The stability analysis is carried out for a linear, scalar law. The stability constraint is generalized to hyperbolic systems at the end of the appendix.

B.1. Analysis for a scalar law

Consider the linear advection equation in two dimensions of space:

$$\frac{\partial U}{\partial t} + v_x \frac{\partial U}{\partial x} + v_y \frac{\partial U}{\partial y} = 0 \tag{B1}$$

where v_x and v_y are the (assumed constant for the present analysis) x and y components of the advection velocity, respectively. Equation (B1) is discretized on a regular, triangular grid (Figure B1) as a particular case of the vector equation (7)

$$U_i^{n+1} = U_i^n - \frac{\Delta t}{A_i} \sum_{k=1}^{3} [v_x n_k^{(x)} + v_y n_k^{(y)}] W_k U_{i,k}^{n+1/2} \tag{B2}$$

where $U_{i,k}^{n+1/2}$ is the value of U at the kth edge of the cell i between the time levels n and $n+1$ and W_k is the length of the kth edge. Two cases must be considered in the present analysis:

DOI: 10.1002/fld

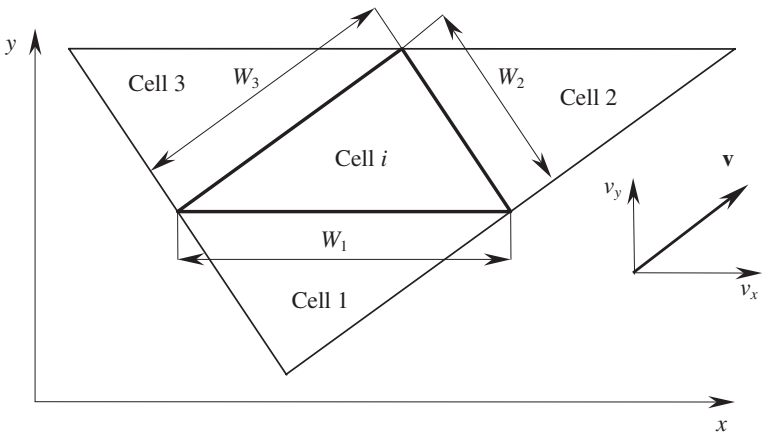

Figure B1. Definition sketch for the stability analysis.

(i) the flow enters the cell i through only one edge and (ii) the flow enters the cell through two edges.

B.1.1. First case. Assume first that the flow enters the cell through only one edge. Without loss of generality, it can be assumed that the coordinate system (x, y) has been chosen such that the flow is entering the cell i through the edge $k = 1$ and leaves the cell through the edges $k = 2$ and 3. Moreover, (x, y) can be adjusted such that the edge $k = 1$ is parallel to x. If this is not the case, the coordinate system can be changed and the cells renumbered in such a way that this condition is satisfied. Then, the values of U at the cell edges are given by

$$\begin{aligned} U_{i,1}^{n+1/2} &= U_1^n \\ U_{i,2}^{n+1/2} &= U_i^n \\ U_{i,3}^{n+1/2} &= U_i^n \end{aligned} \tag{B3}$$

where U_1^n is the average value of U in the cell on the other side of the first edge of the cell i. Substituting Equation (B3) into Equation (B2) gives

$$\begin{aligned} U_i^{n+1} = U_i^n - \frac{\Delta t}{A_i}[&(v_x n_1^{(x)} + v_y n_1^{(y)}) W_1 U_1^n + (v_x n_2^{(x)} + v_y n_2^{(y)}) W_2 U_i^n \\ &+ (v_x n_3^{(x)} + v_y n_3^{(y)}) W_3 U_i^n] \end{aligned} \tag{B4}$$

Since the cell is a triangle, the following equality holds:

$$(v_x n_1^{(x)} + v_y n_1^{(y)}) W_1 + (v_x n_2^{(x)} + v_y n_2^{(y)}) W_2 + (v_x n_3^{(x)} + v_y n_3^{(y)}) W_3 = 0 \tag{B5}$$

DOI: 10.1002/fld

Consequently, Equation (B4) can be rewritten as

$$U_i^{n+1} = U_i^n - \frac{\Delta t}{A_i}[(v_x n_1^{(x)} + v_y n_1^{(y)}) W_1 (U_1^n - U_i^n)] \tag{B6}$$

Since the edge $k = 1$ is assumed parallel to the x direction, Equation (B6) reduces to

$$U_i^{n+1} = U_i^n + \frac{v_y W_1 \Delta t}{A_i}(U_1^n - U_i^n) \tag{B7}$$

In the classical linear stability analysis the solution is sought in the form of a harmonic component

$$U_i^n = U_0 \exp(\mathrm{j}\sigma_x x_i + \mathrm{j}\sigma_y y_i + n\omega\Delta t) \tag{B8}$$

where x_i and y_i are the coordinates of the gravity centre of the cell i, ω is a complex number with a real and imaginary part and j is the pure imaginary number ($\mathrm{j}^2 = -1$). The solution is stable if the modulus of the ratio U_i^{n+1}/U_i^n does not exceed unity. This ratio is easily obtained from Equation (B7)

$$\frac{U_i^{n+1}}{U_i^n} = 1 + \frac{W_1 v_y \Delta t}{A_i}\left(\frac{U_1^{n+1}}{U_i^n} - 1\right) \tag{B9}$$

From Equation (B9) it is possible to define a Courant number Cr_1 in the direction normal to the edge $k = 1$

$$Cr_1 = \frac{W_1 v_y \Delta t}{A_i} \tag{B10}$$

This Courant number is the two-dimensional generalization of the Courant number used for one-dimensional stability analysis. It expresses the ratio of the area of the domain of dependence of the edge $k = 1$ to the area of the cell i. Substituting Equation (B10) into Equation (B9) yields

$$\frac{U_i^{n+1}}{U_i^n} = 1 + \left(\frac{U_1^{n+1}}{U_i^n} - 1\right) Cr_1 \tag{B11}$$

Substituting Equation (B8) into Equation (B11) leads to

$$\frac{U_i^{n+1}}{U_i^n} = 1 + \{\exp[(x_1 - x_i)\mathrm{j}\sigma_x + (y_1 - y_i)\mathrm{j}\sigma_y] - 1\} Cr_1 \tag{B12}$$

This equation can be rewritten as

$$A_N = 1 + \{\exp(\mathrm{j}\theta) - 1\} Cr_1 \tag{B13}$$

where the so-called amplification factor A_N and the angle θ are defined as

$$A_N = \frac{U_i^{n+1}}{U_i^n}$$
$$\theta = (x_1 - x_i)\sigma_x + (y_1 - y_i)\sigma_y \tag{B14}$$

The location of the amplification factor in the complex plane is a circle of radius Cr_1 that is tangent to the unit circle at the point $z = 1$ (Figure B2). A_N remains inside the unit circle if Cr_1 is between

DOI: 10.1002/fld

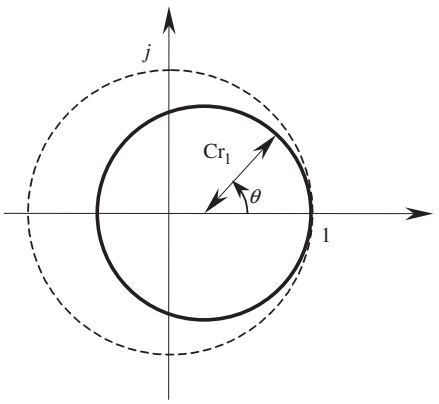

Figure B2. Location of the amplification factor in the complex plane (bold circle) in the first case.

0 and 1. Note that negative values of Cr_1 are meaningless because the velocity v_y was assumed positive at the beginning of this analysis. Therefore, the solution is stable if Cr_1 is smaller than or equal to 1. In other words, a necessary condition for stability is that the area of the domain of dependence of the edge $k=1$ should be smaller than the area of the cell i.

B.1.2. Second case. Consider now the case where the flow enters the cell through two edges. The coordinate system (x, y) is redefined and the edges are renumbered in such a way that the flow is entering the cell i trough the edges $k=2$ and 3 and leaves the cell through the edge $k=1$. As in the previous case, the edge $k=1$ is parallel to the x-axis. Then it is easy to check that

$$\begin{aligned} U_{i,1}^{n+1/2} &= U_i^n \\ U_{i,2}^{n+1/2} &= U_2^n \\ U_{i,3}^{n+1/2} &= U_3^n \end{aligned} \tag{B15}$$

Substituting Equations (B15) and (B5) into Equation (B2) yields

$$U_i^{n+1} = U_i^n - \frac{\Delta t}{A_i}[(v_x n_2^{(x)} + v_y n_2^{(y)}) W_2 (U_2^n - U_i^n) + (v_x n_3^{(x)} + v_y n_3^{(y)}) W_3 (U_3^n - U_i^n)] \tag{B16}$$

Dividing Equation (B16) by U_i^n leads to

$$A_N = 1 + Cr_2 \left(\frac{U_2^n}{U_i^n} - 1 \right) + Cr_3 \left(\frac{U_3^n}{U_i^n} - 1 \right) \tag{B17}$$

where the Courant numbers Cr_2 and Cr_3 are defined as

$$\begin{aligned} Cr_2 &= \frac{W_2 \Delta t}{A_i} (v_x n_2^{(x)} + v_y n_2^{(y)}) \\ Cr_3 &= \frac{W_3 \Delta t}{A_i} (v_x n_3^{(x)} + v_y n_3^{(y)}) \end{aligned} \tag{B18}$$

DOI: 10.1002/fld

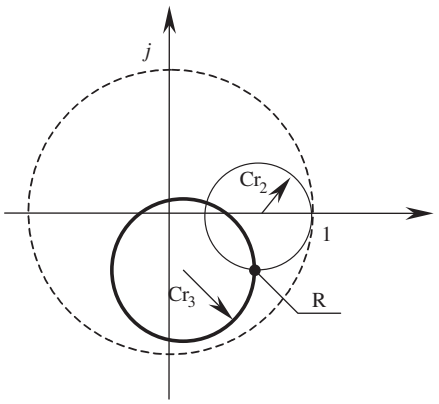

Figure B3. Location of the amplification factor in the complex plane (bold circle) in the second case.

These Courant numbers represent the ratio of the domains of dependence of the edges $k=2$ and 3 to the area of the cell. Equation (B17) can also be rewritten in the form

$$A_N = 1 + Cr_2[\exp(\mathrm{j}\theta_2) - 1] + Cr_3[\exp(\mathrm{j}\theta_3) - 1] \tag{B19}$$

The location of A_N in the complex plane is that of a circle of radius Cr_3, the rightmost point R of which slides on the circle of radius Cr_2 tangent to the unit circle (Figure B3). Obviously, A_N remains inside the unit circle provided that the sum $Cr_2 + Cr_3$ remains smaller than unity.

B.1.3. Generalization of the stability criterion in the scalar case. The two cases above can be accounted for by the following criterion: stability is ensured if the total area of the domains of dependence of all the waves entering the cell i is smaller than the area of the cell i. In other words, the sum of the Courant numbers of the waves entering the cell i should not exceed unity.

B.2. Generalization to hyperbolic systems of conservation laws

When a hyperbolic system of conservation laws is to be solved, the stability analysis must be applied to all the waves in the system. As indicated by Equation (27), the conserved variable is a linear combination of the wave strengths $\alpha^{(p)}$. Each wave strength $\alpha^{(p)}$ is transported at a speed $\lambda^{(p)}$ in the direction normal to the cell interface. Therefore, in Equation (B1) the variable U should be replaced with $\alpha^{(p)}$ and the velocity $\mathbf{v}$ should be replaced with a vector of norm $\lambda^{(p)}$ normal to the cell edges. The numerical solution remains stable if all the wave strengths remain stable. Therefore the stability criterion in the scalar case should hold for the faster of the three waves. Note that when the flow is subcritical, there is at least one wave entering the cell per cell edge. In order to avoid tedious testing procedures that would slow down the computation, the following sufficient condition has been implemented in the present calculations:

$$\frac{[(u^2+v^2)^{1/2}+c](W_1+W_2+W_3)\Delta t}{A_i} \leqslant 1 \quad \text{for all } i \tag{B20}$$

where u and v are the x and y components of the velocity in the cell i, and $c=(gh)^{1/2}$ is the propagation speed of the waves in still water in the cell i. Since Equation (B20) overestimates the

DOI: 10.1002/fld

sum of the areas of the domains of dependence of the waves entering the cell i, it gives a sufficient condition for stability.

ACKNOWLEDGEMENTS

This work was partly supported by Grant No. 2004/V 6/5/009-M 14/9/5-CS-20372 (Bourse de séjour scientifique) from the Fonds National de la Recherche Scientifique (FNRS), Belgium.

REFERENCES

1. Godunov SK. A difference method for numerical calculation of discontinuous equations of hydrodynamics. *Matematicheski Sbornik* 1959; **47**:271–300.
2. Van Leer B. Toward the ultimate conservative difference scheme, IV: A new approach to numerical convection. *Journal of Computational Physics* 1977; **23**:276–299.
3. Colella P, Woodward PR. The piecewise parabolic method (PPM) for gas-dynamical simulations. *Journal of Computational Physics* 1984; **54**:174–201.
4. Toro EF. *Riemann Solvers and Numerical Methods for Fluid Dynamics* (2nd edn). Springer: Berlin, 1999.
5. LeVeque R. *Finite-Volume Methods for Hyperbolic Problems*. Cambridge University Press: Cambridge, MA, 2002.
6. Van Leer B. Towards the ultimate conservative difference scheme IV. A new approach to numerical convection. *Journal of Computational Physics* 1979; **32**:101–136.
7. Hubbard ME. Multidimensional slope limiters for MUSCL-type finite volume schemes on unstructured grids. *Journal of Computational Physics* 1999; **155**:54–74.
8. Billet G, Louedin O. Adaptive limiters for improving the accuracy of the MUSCL approach for unsteady flows. *Journal of Computational Physics* 2001; **170**:161–183.
9. Alcrudo F, Garcia-Navarro P. A high resolution Godunov-type scheme in finite volumes for the 2D shallow-water equations. *International Journal for Numerical Methods in Fluids* 1993; **16**:489–505.
10. Ben-Artzi M, Falcovitz J. A second-order Godunov-type scheme for compressible fluid dynamics. *Journal of Computational Physics* 1984; **55**:1–32.
11. Guinot V. The discontinuous profile method for simulating two-phase flow in pipes using the single-component approximation. *International Journal for Numerical Methods in Fluids* 2001; **37**:341–359.
12. Guinot V. An unconditionally stable, explicit Godunov scheme for systems of conservation laws. *International Journal for Numerical Methods in Fluids* 2002; **38**:567–588.
13. Guinot V. The time-line interpolation method for large-time-step Godunov-type schemes. *Journal of Computational Physics* 2002; **177**:394–417.
14. Guinot V. *Godunov-Type Schemes. An Introduction for Engineers*. Elsevier: Amsterdam, 2003.
15. Strang G. On the construction and comparison of difference schemes. *SIAM Journal on Numerical Analysis* 1968; **5**:506–517.
16. Bell JB, Dawson CN, Shubin GR. An unsplit, higher-order Godunov method for scalar conservation laws in multiple dimensions. *Journal of Computational Physics* 1988; **74**:1–24.
17. Dai W, Woodward PR. A second-order unsplit Godunov scheme for two- and three-dimensional Euler equations. *Journal of Computational Physics* 1997; **134**:261–281.
18. Ben-Artzi M. Application of the generalised Riemann problem method to 1-D incompressible flow with interfaces. *Journal of Computational Physics* 1986; **65**:170–178.
19. Lax PD. Hyperbolic systems of conservation laws II. *Communications on Pure and Applied Mathematics* 1957; **10**:537–566.
20. Colella P. Glimm's method for gas dynamics. *SIAM Journal on Scientific and Statistical Computing* 1982; **3**:76–110.
21. Dukowicz J. A general, non-iterative Riemann solver for Godunov's method. *Journal of Computational Physics* 1985; **61**:119–137.
22. Guinot V. Riemann solvers for water hammer simulations by Godunov method. *International Journal for Numerical Methods in Engineering* 2000; **49**:851–870.
23. Guinot V. Numerical simulations of two-phase flow in pipes using Godunov method. *International Journal for Numerical Methods in Engineering* 2001; **50**:1169–1189.

DOI: 10.1002/fld

24. Soares-Frazão S, Zech Y. Dam-break in channels with 90° bend. *Journal of Hydraulic Engineering* 2002; **128**:956–968.
25. Soares-Frazão S, Spinewine B, Zech Y. Digital-imaging velocity measurements and numerical modelling of a dam-break flow through a 90° bend. *Proceedings of 29th IAHR Congress*, Beijing, China, September 2001; 240–245.
26. Soares-Frazão S, Zech Y. Effects of a sharp bend on dam-break flow. *Proceedings of 28th IAHR Congress*, Graz, Austria (CD-ROM Proceedings), Technical University Graz, Institute for Hydraulics and Hydrology, 1999.
27. Stoker JJR. *Water Waves*. Interscience: New York, 1957.

DOI: 10.1002/fld